Clays and Clay Minerals, Vol. 67, No. 4:348–356, 2019

PHOTO-ASSISTED CATALYTIC REMOVAL OF NO_X OVER $LA_{1-X}PR_XCOO_3$/PALYGORSKITE NANOCOMPOSITES: ROLE OF PR DOPING

Kenian Wei[1,2], Xiangyu Yan[2], Shixiang Zuo[2], Wei Zhu[2], Fengqin Wu[2], Xiazhang Li[2], Chao Yao[2]*, and Xiaoheng Liu[1]

[1]Key Laboratory for Soft Chemistry and Functional Materials, Nanjing University of Science and Technology, Ministry of Education, Nanjing 210094, China

[2]Advanced Catalysis and Green Manufacturing Collaborative Innovation Center, School of Petrochemical Engineering, Changzhou University, Changzhou 213164, China

Abstract—Photo-assisted selective catalytic reduction (photo-SCR) has been considered as a promising strategy for NO_x removal in recent decades. The purpose of the present work was to test the effectiveness of $La_{1-x}Pr_xCoO_3$, supported on the surface of natural palygorskite (Pal) by a facile sol-gel method, as a photo-SCR for the removal of NO_x from wastewaters. The structure, acidity, and the redox property of the prepared $La_{1-x}Pr_xCoO_3$/Pal nanocomposite were characterized using X-ray diffraction (XRD), scanning electron microscopy (SEM), transmission electron microscopy (TEM), UV-Visible diffuse reflectance spectroscopy (UV-Vis DRS), and X-ray photoelectron spectroscopy (XPS). Density functional theory (DFT) calculations were employed to determine the valence bands. The $La_{1-x}Pr_xCoO_3$/Pal catalysts were then tested for SCR removal of NO_x with the assistance of photo-irradiation. The photo-SCR results revealed that the NO_x conversion and the N_2-selectivity were greatly improved by this method and reached >95% when carried out at the relatively low temperature of 200°C and with the Pr doping at $x = 0.5$. The improvements were attributed to the co-precipitation of a $PrCoO_3$ phase as in a solid solution forming a coherent heterojunction of $PrCoO_3/La_{0.5}Pr_{0.5}CoO_3$ on the Pal surface.

Keywords—Low-temperature · NO_x reduction · Palygorskite · Perovskite · Photo-SCR

INTRODUCTION

Nitrogen oxide (NO_x) is a significant pollutant and is a cause of a number of serious environmental problems including acid rain and atmospheric haze (Geng et al. 2017; Xiao et al. 2018). Developing a treatment for NO_x is, therefore, critically important. Selective catalytic reduction has been studied extensively and is used commonly for NO_x removal at high temperature (300–400°C); this process has comparatively high costs and undesirable by-products, however. To solve these problems, photo-assisted selective catalytic reduction (photo-SCR) of NO_x with NH_3 using semiconductor catalysts under the conditions of photo-illumination and low temperature is proposed as a possible alternative for NO_x reduction (Yu et al. 2017).

The structure of perovskite is ABO_3 where A is usually a lanthanide or alkaline earth metal ion, and B is a transition metal ion. Rare- or alkaline-earth elements provide mechanical resistance to the perovskite while transition metals improve the reactivity in redox processes (Cai et al. 2018). Perovskite has a narrow bandgap and good photoresponse to visible light. Due to the flexible alternation of A or B sites, perovskite has been studied widely in photocatalysis (Bhaskar et al. 2017; Humayun et al. 2018). As a typical perovskite, $LaCoO_3$ is easy to agglomerate because of its nano-size particles and large surface energy. Natural clay minerals are considered to offer potential as effective catalyst carriers because of their unique pore structure and layer structure (Zhou & Keeling 2013; Zhou et al. 2016; Chen et al. 2016; Zhu et al. 2019). Palygorskite (Pal), a naturally occurring, fibrous clay mineral, is an excellent example of such a supporting material in catalysts (Li et al. 2017; Liu et al. 2017; Wang et al. 2018) because of its large specific surface area, which inhibits the aggregation of particles, and good adsorption performance (Kadir et al. 2017; Lin et al. 2017]. The purpose of the present study was to measure the effectiveness of $La_{1-x}Pr_xCoO_3$/Pal nanocomposites, synthesized using a facile sol-gel approach, as a photo-assisted SCR of NO_x with NH_3, including an investigation of the effect of Pr doping on the conversion rate and the N_2 selectivity.

EXPERIMENTAL

Chemicals

$La(NO_3)_3{\cdot}6H_2O$, $C_6H_8O_7{\cdot}H_2O$, $Pr(NO_3)_3{\cdot}6H_2O$, and $Co(NO_3)_3{\cdot}6H_2O$ were provided by Sinopharm Chemical Reagent Co., Ltd. (Shanghai, China). Palygorskite was supplied by Jiangsu Nanda Zijin Technology Group Co., Ltd. (Changzhou, China). Citric acid and ethylene glycol were purchased from Shanghai Ling Feng Chemical Reagent Co., Ltd. (Shanghai, China). All reagents were of analytical grade and used without further purification.

Synthesis of $La_{1-x}Pr_xCoO_3$/Pal

$La_{1-x}Pr_xCoO_3$/Pal nanocomposites were prepared by the facile sol-gel method which is summarized briefly as follows: 1.34 g of lanthanum nitrate, 0.12 g of cobalt nitrate, 1.50 g of

* E-mail address of corresponding author: yaochao420@163.com
DOI: 10.1007/s42860-019-00032-1

This paper was originally presented during the World Forum on Industrial Minerals, held in Qing Yang, China, October 2018

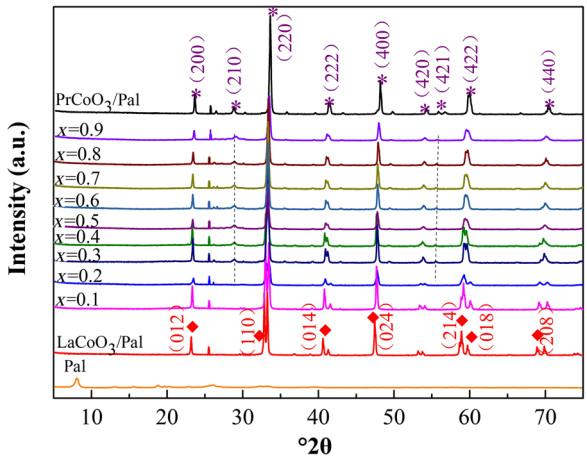

Fig. 1 XRD patterns of $LaCoO_3$/Pal, $PrCoO_3$/Pal, and $La_{1-x}Pr_xCoO_3$/Pal (x = 0–1) Figure 2 blurry text inside the artwork.Dear editor, yes, it is.

praseodymium nitrate, and 1.80 g citric acid were mixed in a 250.0 mL beaker, giving x = 0.1. As these ratios were changed to yield varying values for x, the amount of nitrate also changed. The mixture was dissolved in 10.0 mL of deionized water under ultrasonication. The relative amounts of La and Pr, i.e. the value of x, varied from 0.1 to 0.9. The mixed solution was maintained at 80°C with stirring for 1 h, followed by the addition of 1.0 g of Pal. The composite catalyst was obtained after calcining at 650°C for 2 h.

Characterization

The TEM images were obtained using a transmission electron microscope (JEM–2100, JEOL, Tokyo, Japan), working at 200 kV. The XRD patterns were captured using a Rigaku D/Max-2500 X-ray diffractometer equipped with a Cu anode (Rigaku Corporation, Tokyo, Japan), running at 60 kV and 30 mA between the angles of 10 and 80°2θ at a scan rate of 0.05°2θ/s. The Fourier-transform infrared (FTIR) spectra were

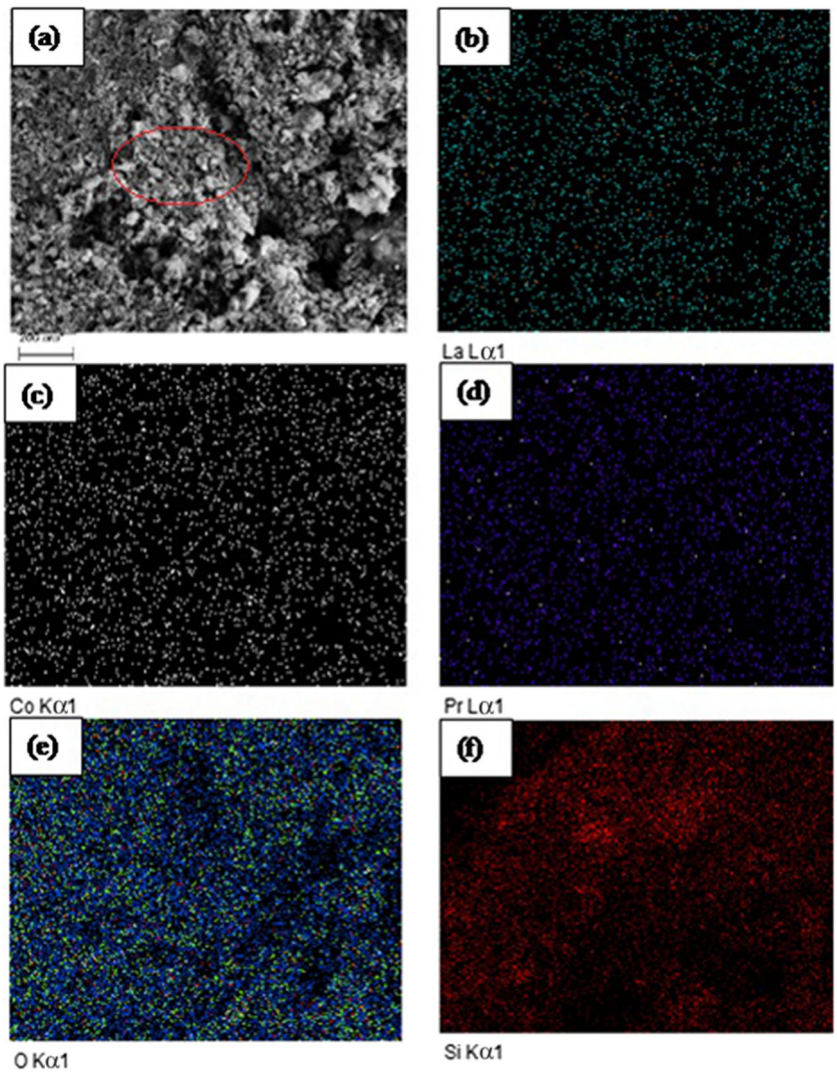

Fig. 2 SEM images and element distribution of $La_{0.5}Pr_{0.5}CoO_3$/Pal

https://doi.org/10.1007/s42860-019-00032-1 Published online by Cambridge University Press

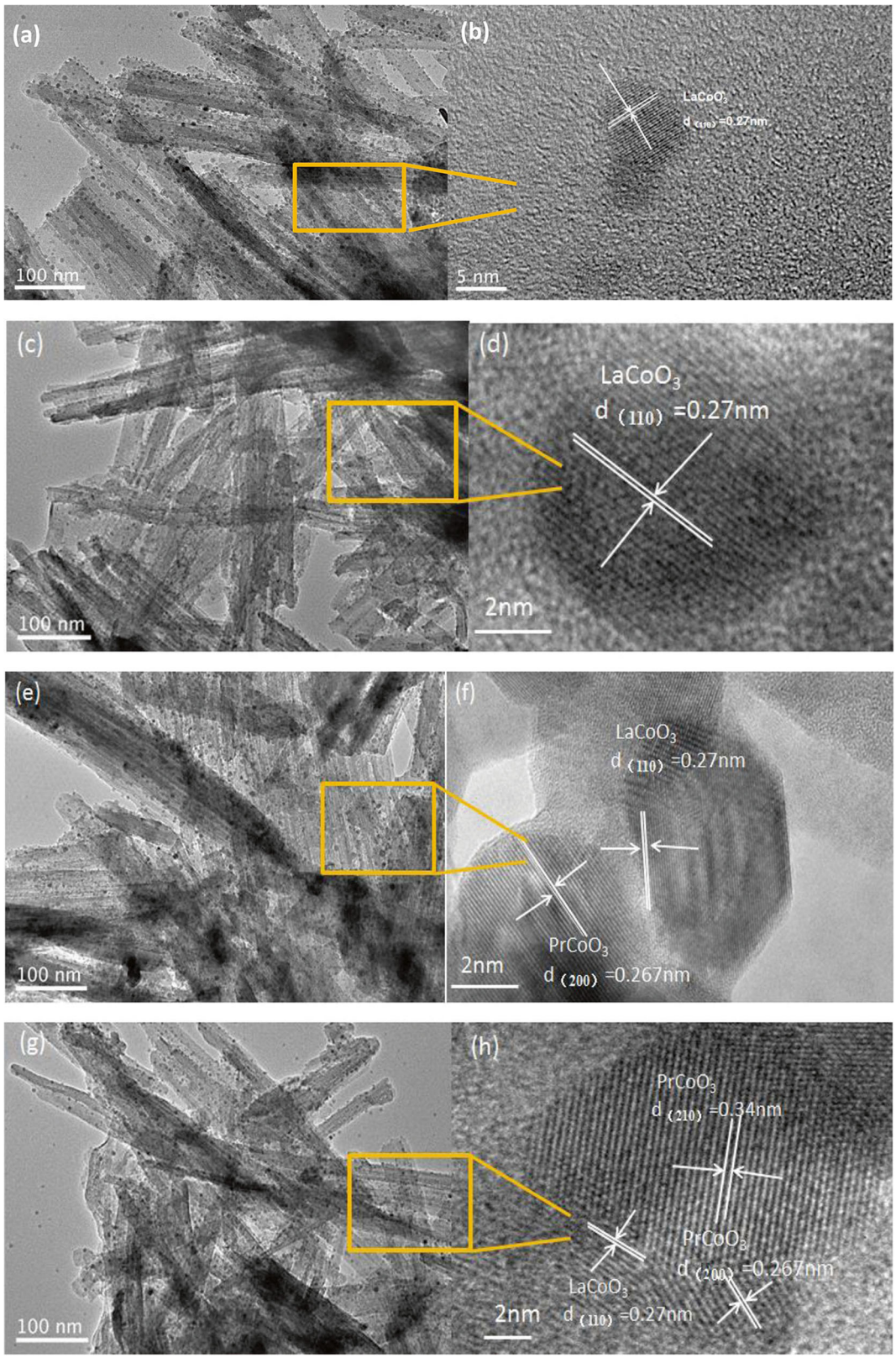

Fig. 3 TEM photomicrographs of $La_{1-x}Pr_xCoO_3$/Pal (x = 0.1, 0.3, 0.5, or 0.7)

https://doi.org/10.1007/s42860-019-00032-1 Published online by Cambridge University Press

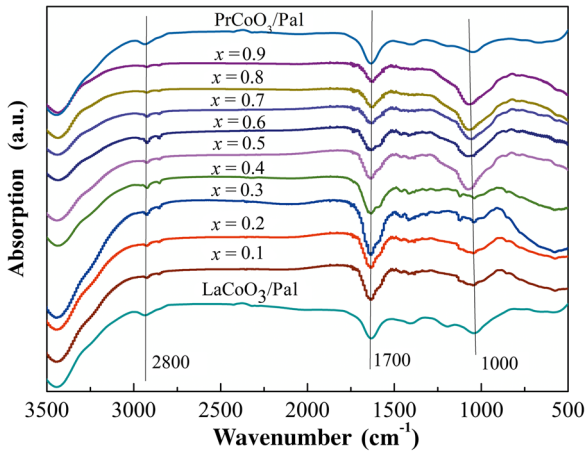

Fig. 4 FTIR spectra of $La_{1-x}Pr_xCoO_3$/Pal (x = 0–1)

measured using a PerkinElmer Spectrum 100 FT-IR spectrometer (PerkinElmer, Shelton, Connecticut, USA).

The total acidity and acid distribution of the catalysts were measured by means of the temperature-programmed desorption (TPD) of NH_3 using a Micromeritics (Norcross, Georgia, USA) ASAP 2920 instrument equipped with a thermal conductivity detector (TCD). A sample of the $La_{1-x}Pr_xCoO_3$/Pal nanocomposite (sieved to 0.2–0.3 mm, 0.3 g) was added to a fixed-bed flow reactor using N_2 as the flow gas. The sample was degassed at 400°C for 30 min, and then cooled to room temperature (~25°C). A flow (30 mL/min) of NH_3 was introduced for 30 min followed by a purge with N_2 to remove the physically adsorbed NH_3 on the catalyst surface. TPD of chemically adsorbed NH_3 was then carried out under N_2 flow (50 mL/min) at 25–500°C with a heating rate of 10°C/min.

Temperature-programmed reduction by hydrogen (H_2-TPR) was performed using the same Micromeritics ASAP 2920 instrument as for TPD. Samples of ~50 mg were heated from ambient temperature to 700°C at 10°C/min in a reducing atmosphere of H_2 mixed (10 vol.%) with Ar (flow rate of 30 mL/min).

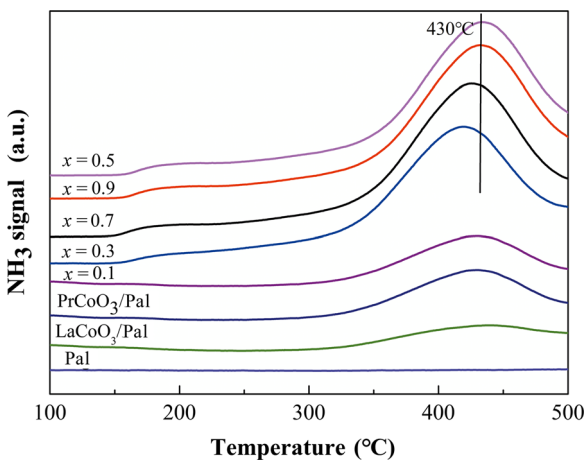

Fig. 5 NH_3-TPD of $La_{1-x}Pr_xCoO_3$/Pal (x = 0.1, 0.3, 0.5, 0.7, or 0.9)

XPS measurements (Thermo Fisher Scientific, Waltham, Massachusetts, USA) were carried out using a Quantum 2000 Scanning ESCA Microprobe instrument using Al Kα. The C1s signal was set to a position of 284.6 eV.

Photo-SCR performance

The photo-SCR catalytic experiments were carried out in a fixed-bed reactor operated in a steady-state flow mode. A 500 W Xenon lamp was employed to provide a light source irradiation to simulate solar light. A UV-filter was placed at both ends of the window to cut off wavelengths <420 nm to guarantee only visible light irradiation. The catalyst temperature was measured through a thermocouple projecting into the center of the reactor. The reactant gas consisted of 1000 ppm NO, 1000 ppm NH_3, and 3 vol.% O_2, with the balance being N_2, which follows the conditions of "practical" SCR (Li et al. 2018). The total flow rate was adjusted to 1 L/min by the mass flow control corresponding to a GHSV (gas hourly space velocity) of 40,000 h^{-1}. A flue gas analyzer (KM9106, Kane International, Ltd., Welwyn Garden City, UK) was used to measure the inlet and outlet concentrations of NO_x. The concentration of gas was recorded once every 5 min during the reaction. The main photo-SCR reaction was

$$NO + NH_3 + \frac{1}{4O_2} \rightarrow N_2 + 3/2H_2O \quad (1)$$

The N_2 selectivity was calculated from

$$N_2\ \text{selectivity} = \left(1 - \frac{2[N_2O]_{outlet}}{[NO_x]_{inlet} + [NH_3]_{inlet} - [NO_x]_{outlet} - [NH_3]_{outlet}}\right) \times 100\% \quad (2)$$

RESULTS AND DISCUSSIONS

XRD and BET Analysis

In the XRD patterns of pure Pal, $LaCoO_3$, and $La_{1-x}Pr_xCoO_3$/Pal (Fig. 1), the characteristic diffraction peak at 8.3°2θ corresponded to the (110) crystal plane of Pal. The intensity of this peak decreased gradually, indicating that rare-earth perovskite had been loaded successfully onto the surface of Pal (Takase et al. 2018). When x was 0, the diffraction peaks at 22.86, 32.51, 40.12, 46.70, 57.87, 68.08, and 77.39°2θ corresponded to the (012), (110), (014), (024), (214), (018), and (208) crystal planes of $LaCoO_3$, respectively (JCPDS Card, NO.48-123). The diffraction peaks at 23, 26, 33, 41, 48, 59, 70, and 80°2θ corresponded to the (200), (210), (220), (222), (400), (422), (440), and (620) crystal planes of $PrCoO_3$, respectively (JCPDS Card NO.25-1069). As the amount of Pr doping increased, the main peak (110) of perovskite was weakened gradually. When the doping amount was 0.5, $PrCoO_3$ was precipitated. With further increase in Pr doping, the characteristic peaks of $PrCoO_3$ at 32°2θ shifted progressively to a higher Bragg angle, which might be due to the fact that the Pr^{3+} radius is smaller than that of the La^{3+}.

https://doi.org/10.1007/s42860-019-00032-1 Published online by Cambridge University Press

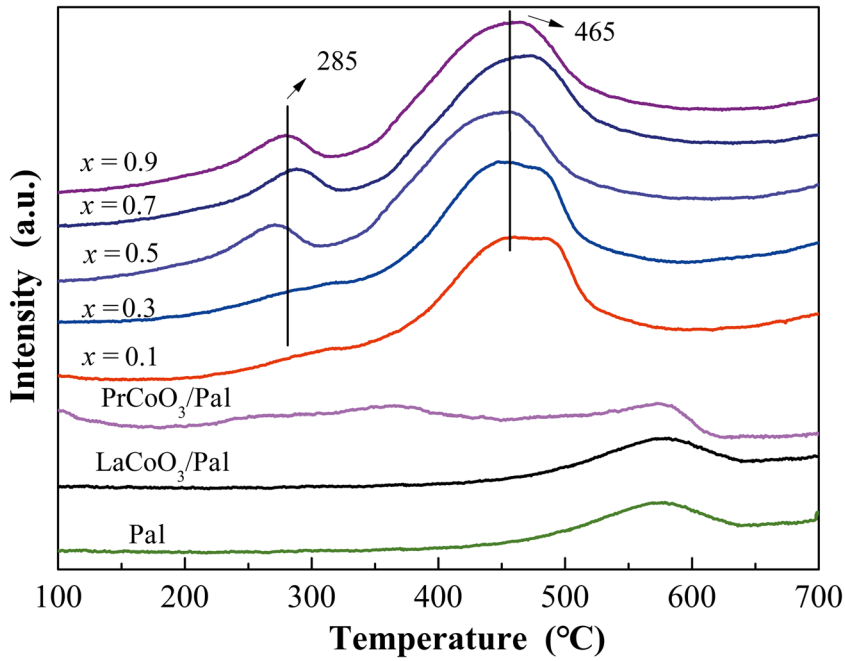

Fig. 6 H_2-TPR of $La_{1-x}Pr_xCoO_3$/Pal (x = 0.1, 0.3, 0.5, 0.7, or 0.9)

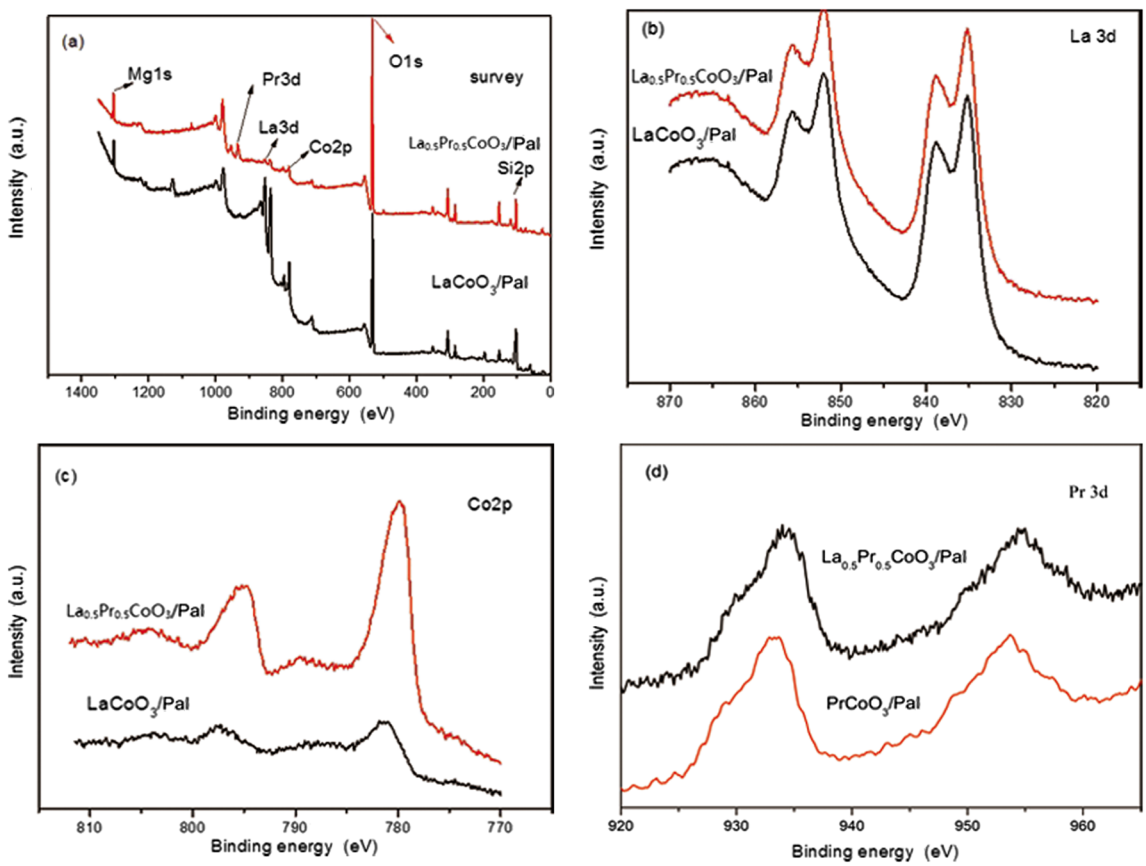

Fig. 7 (a) XPS survey full scan spectra of $LaCoO_3$/Pal and $La_{0.5}Pr_{0.5}CoO_3$/Pal. XPS high-resolution scans of $LaCoO_3$/Pal and $La_{0.5}Pr_{0.5}CoO_3$/Pal binding energies of (b) La 3d, (c) Co 2p, and (d) Pr 3d

https://doi.org/10.1007/s42860-019-00032-1 Published online by Cambridge University Press

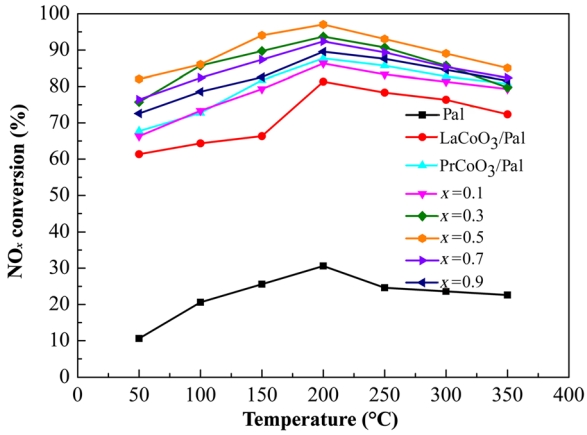

Fig. 8 Photo-SCR conversion of NO_x by $LaCoO_3$/Pal; $PrCoO_3$/Pal; and $La_{1-x}Pr_xCoO_3$/Pal (x = 0.1, 0.3, 0.5, 0.7, or 0.9)

Some Pr^{3+} ions entered into the lattice of $LaCoO_3$, leading to lattice distortion and, as a result, the tolerance factor value of the crystal structure decreased. Meanwhile, some $PrCoO_3$ might precipitate and accumulate on the surface of $LaCoO_3$. The main peak of $PrCoO_3$ coincided with that of partial Pal (the Pal part of $PrCoO_3$/Pal composites) which was not identified in the XRD spectrum. In addition, Pal had the largest specific surface area (S_{BET} = 127.74 m^2/g) and the largest pore volume (V_t = 0.48 cm^3/g) in all materials ($La_{1-x}Pr_xCoO_3$/Pal, x = ~0.1–0.9). After loading $LaCoO_3$ and $La_{0.5}Pr_{0.5}CoO_3$, the specific surface area (S_{BET} = 101.01 m^2/g and 97.18 m^2/g) and pore volume (V_t = 0.34 cm^3/g and 0.21 cm^3/g) of $LaCoO_3$/Pal and $La_{0.5}Pr_{0.5}CoO_3$/Pal decreased significantly. However, the pore size of $LaCoO_3$/Pal and $La_{0.5}Pr_{0.5}CoO_3$/Pal (d = 16.51 and 18.05 nm) was larger than that of Pal (d = 15.83 nm) because a large number of micropores and mesopores disappeared with the loading of $LaCoO_3$ and $La_{0.5}Pr_{0.5}CoO_3$. The pore size of the material generally appeared to increase. Therefore, in combination with the XRD results, $La_{1-x}Pr_xCoO_3$ was supported successfully on the surface of Pal.

SEM Analysis

A field emission scanning electron micrograph (FE-SEM) of the composite photocatalyst showed significant agglomeration at low resolution (Fig. 2a). Particles of various sizes and with many channels among the particles were observed and attributed to the accumulation of $PrCoO_3$ on the surface of Pal. The element mapping distribution of the $La_{1-x}Pr_xCoO_3$/Pal composites (Fig. 2b–2f) illustrated that the distribution of each element was relatively uniform, which was beneficial in that it improved the degradation of NO_x by the photo-SCR.

TEM Analysis

Transmission electron microscopy images of $La_{1-x}Pr_xCoO_3$/Pal composites under various levels of doping (x = 0.1, 0.3, 0.5, and 0.7) depicted the process of formation of the $PrCoO_3/La_{1-x}Pr_xCoO_3$ heterostructure (Fig. 3). The diameter of Pal particles was 20–40 nm and the fiber length was ~800 nm (Fig. 3a,c). The nanoparticles of $LaCoO_3$ were scattered uniformly on the surface of Pal without significant agglomeration. The diameter of the $LaCoO_3$ nanoparticles was 10–25 nm (Fig. 3b,d). The lattice spacing of $LaCoO_3$ nanoparticles on the surface of Pal was 0.27 nm, corresponding to the (110) plane of $LaCoO_3$ (Wang et al. 2017). The nanoparticles of $La_{0.5}Pr_{0.5}CoO_3$ were distributed uniformly on the surface of Pal without obvious agglomeration and the average size of the particles was ~10 nm (Fig. 3e). The existence of heterojunctions in rare earth perovskite composites was clearly visible (Fig. 3f). The lattice spacing of the nanoparticles was 0.267 nm, corresponding to the (200) plane of $PrCoO_3$, which indicated that $PrCoO_3$ was precipitated. The particles were dispersed uniformly on the surface of Pal (Fig. 3g). A new phase of $PrCoO_3$ appeared, as evidenced by the (200) and (210) crystal planes (Fig. 3h), and was due to the conversion of the composite catalyst to pure $PrCoO_3$.

FTIR Analysis

The FTIR spectra of $LaCoO_3$/Pal, $PrCoO_3$/Pal, and $La_{1-x}Pr_xCoO_3$/Pal (x = 0–1) showed that the absorption peaks around 787.14 and 3492.18 cm^{-1} were the stretching vibrations of the coordination water from Pal (Fig. 4). The absorption peaks at ~1455.13 and ~1645.85 cm^{-1} corresponded to the stretching vibration of Si-O-Al and zeolite water, respectively (Chen et al. 2018). The peaks at 1700 and 2800 cm^{-1} in $La_{1-x}Pr_xCoO_3$/Pal represented the stretching vibrations of the La–O–Pr bond. Notably, the absorption peaks of $La_{1-x}Pr_xCoO_3$/Pal near 491.23, 1124.38, and 3492.18 cm^{-1} became significantly weaker than those of pure Pal, indicating that $La_{1-x}Pr_xCoO_3$ was dispersed evenly on the Pal surface. The results above were consistent with the TEM results.

NH_3-TPD Analysis

The temperature programmed adsorption (TPA) patterns of pure Pal were linear and independent of temperature (Fig. 5), indicating that the adsorption capacity of NH_3 gas for Pal was small compared with that of the $La_{1-x}Pr_xCoO_3$/Pal. However, weak peaks from $LaCoO_3$/Pal and $PrCoO_3$/Pal appeared at ~430°C, indicating that these two composites possessed minor

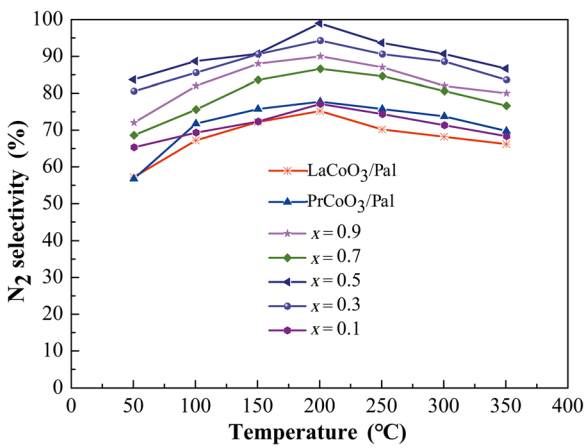

Fig. 9 N_2 selectivity of $LaCoO_3$/Pal; $PrCoO_3$/Pal; and $La_{1-x}Pr_xCoO_3$/Pal (x = 0.1, 0.3, 0.5, 0.7, or 0.9)

https://doi.org/10.1007/s42860-019-00032-1 Published online by Cambridge University Press

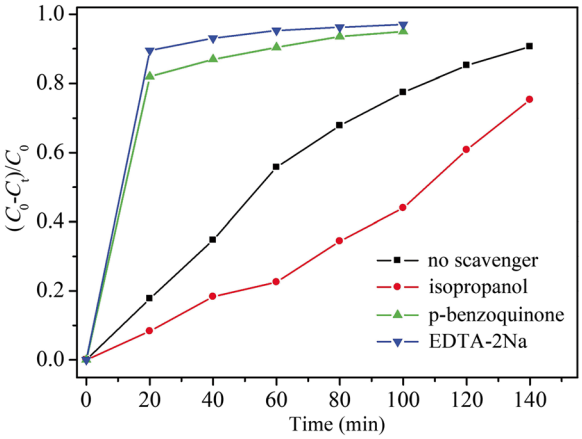

Fig. 10 DFT calculations in the presence of various scavengers for (a) $LaCoO_3$, (b) $PrCoO_3$, (c) $La_{0.5}Pr_{0.5}CoO_3$, and (d) the unit crystal cell of $La_{0.5}Pr_{0.5}CoO_3$. Atoms: green — La, blue — Pr, red — O, brown – Co

acidic sites. With increased Pr doping, the intensity of the peak at ~430°C was enhanced gradually. Meanwhile, as the doping level of Pr increased, the peak shifted to higher temperatures and the peak intensity increased. When x was 0.5, the peak showed greatest intensity, indicating that $La_{0.5}Pr_{0.5}CoO_3$/Pal had the most acidic sites, which was beneficial to the SCR reaction. When the doping amount was >0.5, the peak intensity became weaker and the number of acid sites decreased.

H_2-TPR Analysis

The H_2-TPR patterns of pure Pal and $La_{1-x}Pr_xCoO_3$/Pal were also acquired to evaluate the redox activity (Fig. 6). Peaks at 285 and 465°C represented chemisorbed oxygen and lattice oxygen of $La_{1-x}Pr_xCoO_3$, respectively. When x was 0.5, the two peaks of chemisorbed and lattice oxygen shifted to a lower temperature, indicating that $La_{0.5}Pr_{0.5}CoO_3$ was reduced more easily. The restoration process included $Co^{3+} \rightarrow Co^{2+}$ and $Pr^{4+} \rightarrow Pr^{3+}$ (Ayodele et al. 2017). According to the order and peak areas, the $La_{0.5}Pr_{0.5}CoO_3$ composite revealed the optimum redox activity compared with $La_{1-x}Pr_xCoO_3$/Pal composites (x = ~0.1–0.4, and ~0.6–0.9), which was consistent with the low-temperature photo-SCR activity.

XPS Analysis

XPS measurements of pure Pal and $La_{1-x}Pr_xCoO_3$/Pal were employed to obtain more information about elemental identification (Fig. 7). The full scan spectra of $LaCoO_3$/Pal and $La_{0.5}Pr_{0.5}CoO_3$/Pal confirmed the presence of Pr in the $La_{0.5}Pr_{0.5}CoO_3$/Pal (Fig. 7a). The high-resolution XPS spectra of La 3d, Co 2p, and Pr 3d binding energies (Fig. 7b, c, and d, respectively) revealed that the La 3d peak of $La_{0.5}Pr_{0.5}CoO_3$/Pal moved to higher binding energy compared with $LaCoO_3$/Pal (Fig. 7b), which might be due to the difference in ionic radii between Pr and La. The position of the Co 2p peak was virtually unchanged because the doping was in the A site but Co is in the B site (Fig. 7c). Pr 3d yielded two main peaks at binding energies of 935 eV and 955 eV (Fig. 7d), which was consistent with a previous study (Poggio-Fraccari et al. 2018).

NO_x Conversion

Increasing the amount of Pr doping in the $La_{1-x}Pr_xCoO_3$/Pal photo-SCR nanocomposite greatly increased the denitration of NO_x (Fig. 8). The denitration activity of $LaCoO_3$/Pal at 100–250°C increased with increasing temperature. When $x > 0.1$, the denitration activity of $La_{1-x}Pr_xCoO_3$/Pal was greatly improved; in particular, the extent of NO_x elimination by $La_{0.5}Pr_{0.5}CoO_3$/Pal reached 95% at 200°C, a 20% increase over that of $LaCoO_3$/Pal. Some $PrCoO_3$ may have precipitated on the surface of perovskite to generate the heterojunction of $PrCoO_3/La_{1-x}Pr_xCoO_3$, contributing to separation of the photo-induced electron-hole pairs. The conversion of NO decreased with increasing doping levels of $x > 0.5$, and the conversion extent was less than with $LaCoO_3$/Pal.

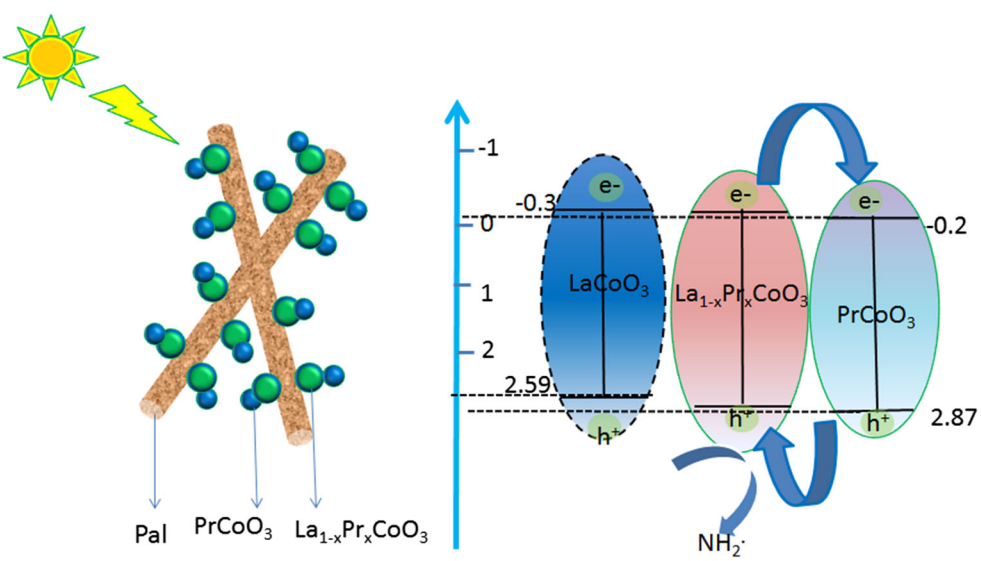

Fig. 11 Schematic illustration of photo-SCR mechanism for $La_{1-x}Pr_xCoO_3$/Pal

https://doi.org/10.1007/s42860-019-00032-1 Published online by Cambridge University Press

Under this circumstance, part of the Pr precipitated to form $PrCoO_3$ which adhered to the surface of rare-earth perovskite and Pal, and hindered the adsorption of NH_3 by the acidic sites of rare-earth perovskite, leading to a reduction of the conversion rate of NO, which was consistent with the results of XRD. From the perspective of denitration effect and economy, $La_{0.5}Pr_{0.5}CoO_3$/Pal composite had the best effect.

N_2 Selectivity

The N_2 selectivity of $LaCoO_3$/Pal and $PrCoO_3$/Pal was ~60–70% (Fig. 9). When $x > 0.1$, the N_2 selectivity began to rise. When $x = 0.5$, the N_2 selectivity reached a maximum value of 99%, which was ascribed to the formation of $PrCoO_3$/$La_{1-x}Pr_xCoO_3$ heterojunction, accelerating the separation of photogenerated electron-hole pairs. However, when $x > 0.5$, the N_2 selectivity of $La_{1-x}Pr_xCoO_3$/Pal began to decrease, which was due to the excessive amount of $PrCoO_3$ precipitated on the surface of $La_{1-x}Pr_xCoO_3$/Pal, hindering further catalytic reaction.

DFT Calculations

DFT calculations of $LaCoO_3$, $PrCoO_3$, $La_{0.5}Pr_{0.5}CoO_3$, and the unit-cell diagram of $La_{0.5}Pr_{0.5}CoO_3$ (Fig. 10) revealed that the band gaps of $LaCoO_3$, $PrCoO_3$, and $La_{0.5}Pr_{0.5}CoO_3$ were 2.89, 2.94, and 3.07 eV, respectively. The Valence Band (VB) values were 2.59, 2.69, and 2.87 eV; and the Conduction Band (CB) values were –0.3, –0.25, and –0.2 eV. In addition, the occurrence of spin up and down should be considered when doing DFT calculations because $LaCoO_3$, $PrCoO_3$, and $La_{0.5}Pr_{0.5}CoO_3$ exhibited specific magnetic properties. From the view of the unit cell of $La_{0.5}Pr_{0.5}CoO_3$ (Fig. 10d), $La_{0.5}Pr_{0.5}CoO_3$ belongs to the orthorhombic system. The space group of La^{3+} and Pr^{3+} is *Pnma*, and the six oxygen atoms around Co^{3+} were arranged in the unit cell. The Co atoms at eight corners of the cuboid, and some La atoms were replaced by Pr atoms, demonstrating the Pr doping.

The Mechanism for the Photo-SCR of $La_{1-x}Pr_xCoO_3$/Pal

On the basis of the above results, a mechanism for the photo-SCR of NO with NH_3 using $La_{1-x}Pr_xCoO_3$/Pal is proposed here (Fig. 11). The microspores of Pal had a physical-adsorption effect on gas enrichment (Yan et al. 2018). Under irradiation by visible light, $La_{1-x}Pr_xCoO_3$ absorbs light to generate electrons (e^-) and holes (h^+). Simultaneously, the electrons shift from the VB to CB of $La_{1-x}Pr_xCoO_3$ and transferred to the surface of $PrCoO_3$, whereas the holes transferred from $PrCoO_3$ to $La_{1-x}Pr_xCoO_3$. The effective charge separation and the separated electrons, therefore, facilitated the reduction of NO on the Pal surface.

CONCLUSIONS

$La_{1-x}Pr_xCoO_3$/Pal nanocomposites with various levels of Pr doping were fabricated successfully by a facile sol-gel approach for the photo-SCR of NO_x with NH_3. Pal was an effective carrier with outstanding adsorption in the process of photo-SCR. Pr doping of $LaCoO_3$ produced an obvious increase in the NO conversion and on the N_2 selectivity. The performance of $La_{0.5}Pr_{0.5}CoO_3$/Pal as a catalyst was excellent, eliminating >95% of the NO_x over the low temperature range of 150–250°C. DFT calculations revealed that Pr incorporated into the $LaCoO_3$ lattice could modulate the band gap forming an intimate and staggered heterojunction of $PrCoO_3/La_{1-x}Pr_xCoO_3$, which enhanced the photo-absorption and facilitated the separation of electron-holes under visible light irradiation.

ACKNOWLEDGMENTS

This work was supported by Fundamental Research Funds for the Central Universities (No. 30916014103), Key R&D Programs of Jiangsu Province (BE2018649) and Innovation Team of Six Talent Peaks of Jiangsu Province (XCL-CXTD-029).

REFERENCES

Ayodele, B. V., Khan, M. R., & Cheng, C. K. (2017). Greenhouse gases mitigation by CO_2 reforming of methane to hydrogen-rich syngas using praseodymium oxide supported cobalt catalyst. *Clean Technologies and Environmental Policy, 19*, 795–807.

Bhaskar, A., Huang, M. S., & Liu, C. J. (2017). Effects of Fe doping on the thermal hysteresis of the $La_{0.5}Ca_{0.5}MnO_3$ system. *RSC Advances, 7*, 11543–11154.

Cai, Y., Zhu, X., Hu, W., Zheng, C., Yang, Y., Chen, M., & Gao, X. (2018). Plasma-catalytic decomposition of ethyl acetate over $LaMO_3$ (M = Mn, Fe, and Co) perovskite catalysts. *Journal of Industrial and Engineering Chemistry*. https://doi.org/10.1016/j.jiec.2018.11.007.

Chen, M., Wang, Y., Yang, Z., Liang, T., Liu, S., Zhou, Z., & Li, X. (2018). Effect of Mg-modified mesoporous Ni/Attapulgite catalysts on catalytic performance and resistance to carbon deposition for ethanol steam reforming. *Fuel, 220*, 32–46.

Chen, L., Zhou, C. H., Fiore, S., Tong, D. S., Zhang, H., Li, C. S., Ji, S. F., & Yu, W. H. (2016). Functional magnetic nanoparticle/clay mineral nanocomposites: preparation, magnetism and versatile applications. *Applied Clay Science, 127-128*, 143–163.

Geng, Y., Chen, X., Yang, S., Liu, F., & Shan, W. (2017). Promotional effects of Ti on a CeO_2-MoO_3 catalyst for the selective catalytic reduction of NO_x with NH_3. *ACS Applied Materials & Interfaces, 9*, 16951–16958.

Humayun, M., Sun, N., Raziq, F., Zhang, X., Yan, R., Li, Z., Qu, Y., & Jing, L. (2018). Synthesis of ZnO/Bi-doped porous $LaFeO_3$ nanocomposites as highly efficient nano-photocatalysts dependent on the enhanced utilization of visible-light-excited electrons. *Applied Catalysis B: Environmental, 231*, 23–33.

Kadir, S., Eren, M., Irkec, T., Erkoyun, H., Kulah, T., Onalgil, N., & Huggett, J. (2017). Lacustrine sediments of the Lower Pliocene Sakarya and Porsuk formations in the Sivrihisar and Yunusemre-Bicer regions (Eskisehir), Turkey. *Clays and Clay Minerals, 65*, 310–328.

Li, X., Shi, H., Wang, T., Zhang, Y., Zuo, S., Luo, S., & Yao, C. (2018). Photocatalytic removal of NO by Z-scheme mineral based heterojunction intermediated by carbon quantum dots. *Applied Surface Science, 456*, 835–844.

Li, X., Yan, X., Zuo, S., Lu, X., Luo, S., Li, Z., Yao, C., & Ni, C. (2017). Construction of $LaFe_{1-x}Mn_xO_3$/attapulgite nanocomposite for photo-SCR of NO_x at low temperature. *Chemical Engineering Journal, 320*, 211–221.

Lin, S., Zhou, T., & Yin, S. (2017). Properties of thermally treated granular montmorillonite-palygorskite adsorbent (GMPA) and use to remove Pb^{2+} and Cu^{2+} from aqueous solutions. *Clays and Clay Minerals, 65*, 184–192.

Liu, Z., Gu, C., Bian, Y., Jiang, X., Sun, Y., Fei, Z., & Dai, J. (2017). Enhanced debromination of decabrominated diphenyl ether in

aqueous solution by attapulgite supported Fe/Ni bimetallic nanoparticles: kinetics and pathways. *Materials Research Express, 4*, 085009.

Xiao, S., Pan, D., Liang, R., Dai, W., Zhang, Q., Zhang, G., Su, C., Li, H., & Chen, W. (2018). Bimetal MOF derived mesocrystal $ZnCo_2O_4$ on rGO with High performance in visible-light photocatalytic NO oxidization. *Applied Catalysis B: Environmental, 236*, 304–313.

Poggio-Fraccari, E., Baronetti, G., & Marino, F. (2018). Pr^{3+} surface fraction in CePr mixed oxides determined by XPS analysis. *Journal of Electron Spectroscopy and Related Phenomena, 222*, 1–4.

Takase, M., Pappoe, A. N., Afrifa, E. A., & Miyittah, M. (2018). High performance heterogeneous catalyst for biodiesel production from non-edible oil. *Renewable Energy Focus, 25*, 24–30.

Wang, T., Chen, Y., Ma, J., Jin, Z., Chai, M., Xiao, X., Zhang, L., & Zhang, Y. (2018). A polyethyleneimine-modified attapulgite as a novel solid support in matrix solid-phase dispersion for the extraction of cadmium traces in seafood products. *Talanta, 180*, 254–259.

Wang, X., Zuo, J., Luo, Y., & Jiang, L. (2017). New route to CeO_2/$LaCoO_3$ with high oxygen mobility for total benzene oxidation. *Applied Surface Science, 396*, 95–101.

Yan, S., Pan, Y., Wang, L., Zhang, X., Liu, J., & Yang, J. (2018). Effects of calcination temperature on the microstructure and adsorption properties of attapulgite microspheres. *Materials Science Forum, 913*, 907–916.

Yu, J. C., Nguyen, V., Lasek, J., & Wu, J. C. (2017). Titania nanosheet photocatalysts with dominantly exposed (001) reactive facets for photocatalytic NO_x abatement. *Applied Catalysis B: Environmental, 219*, 391–400.

Zhou, C. H., & Keeling, J. (2013). Fundamental and applied research on clay minerals: From climate and environment to nanotechnology. *Applied Clay Science, 74*, 3–9.

Zhou, C. H., Zhao, L. Z., Wang, A. Q., Chen, T. H., & He, H. P. (2016). Current fundamental and applied research into clay minerals in China. *Applied Clay Science, 119*, 3–7.

Zhu, T. T., Zhou, C. H., Kabwe, F. B., Wu, Q. Q., Li, C. S., & Zhang, J. R. (2019). Exfoliation of montmorillonite and related properties of clay/polymer nanocomposites. *Applied Clay Science, 169*, 48–66.

[*Received 6 December 2018; revised 27 July 2019; AE: Chun-Hui Zhou*]